Master of Science
Thesis
VT2023

Quantitative susceptibility mapping of the knee: A comparison of approaches for addressing fatty tissue

Cornelia Säll

Supervisors

Emma Einarsson, Pernilla Peterson, and Emelie Lind

Medical Radiation Physics, Lund
Faculty of Science
Lund University
www.msf.lu.se

Populärvetenskaplig sammanfattning

Artros är en vanlig sjukdom som påverkar ett antal olika leder i kroppen. Den vanligaste av dessa är knäartros, som utgör omkring 85 % av alla atrosfall. Sjukdomen påverkar alla delar av leden, speciellt tydlig är effekten på ledbrosket som förtunnas och till slut bryts ner helt. Denna process kan leda till stora besvär, så som smärta och minskad rörlighet, men i nuläget finns mycket få behandlingsalternativ för den som drabbas. För att få en bättre förståelse för sjukdomsförloppet och därigenom förbättra behandlingsmöjligheterna krävs undersökningsmetoder som gör det möjligt att upptäcka tidiga tecken på artros. Tack vare sin goda mjukvävnadskontrast kan undersökning med magnetkamera (MR) vara ett bra alternativ. En relativt ny MR-baserad teknik är mätning av magnetisk susceptibilitet (QSM), som syftar till att från MR-bilder ta reda på vävnaders magnetiska egenskaper.

Magnetisk susceptibilitet beskriver hur ett material reagerar på ett yttre magnetfält, vilket har betydelse för hur magnetfältet runt materialet påverkas. Från material med negativ susceptibilitet kommer en störning av det yttre fältet ske som resulterar i ett lägre magnetiskt fält lokalt, medan material med en positiv susceptibilitet gör motsatsen. Inom MR används en kamera med ett starkt magnetiskt fält, vilket påverkas av susceptibiliteten i materialet som avbildas. Detta utnyttjas inom QSM, där störningar i magnetkamerans fält används för att mäta susceptibiliteten hos materialet som orsakade dem.

QSM har framför allt använts för undersökning av hjärnan, men studier har även gjorts där tekniken använts för bildtagning av knäleden. Problem uppstår dock när QSM ska användas i områden med mycket omkringliggande fettvävnad eftersom MR-signalen från denna stör QSM-beräkningen. Detta har hanterats på olika sätt, antingen genom att korrigera för störningarna som fettet tillför, eller genom att exkludera fettvävnaden från området som ska utvärderas. Båda tillvägagångssätten riskerar att medföra felaktiga mätvärden. Syftet med detta arbete var att jämföra tekniker för att hantera fettvävnad vid QSM-beräkningar i knäleden med hjälp av simuleringar och utvärdering av bilder från MR-undersökningar av knäleder.

Simuleringarna visade att fettvävnad helst ska inkluderas i utvärderingen, då detta ledde till minst fel i beräkningarna. Från utvärderingen av MR-bilderna fann vi att korrektion för fettsignalen måste göras om fettvävnad ska inkluderas, och att felaktigheter i denna korrektion kan resultera i kvarvarande effekter som orsakar störningar av beräkningarna. I utvärderingen av MR-bilder sågs även liknande felaktigheter som i simuleringarna då fettvävnad exkluderades.

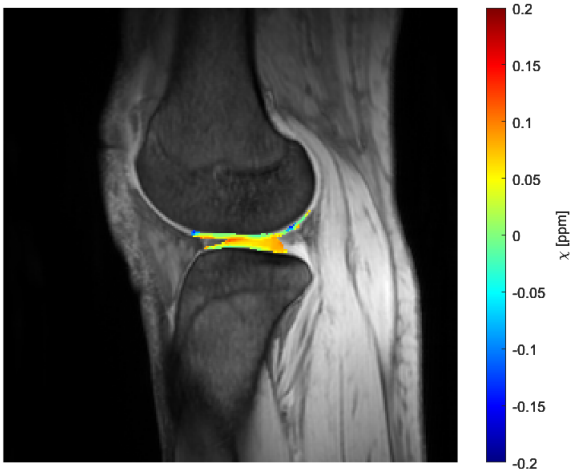

Resultatet av QSM i knäledsbrosk visat över en MR-bild på ett knä, där χ anger susceptibiliteten.

Abstract

Background/purpose

Quantitative susceptibility mapping (QSM) is an MRI-based post processing technique to evaluate the magnetic susceptibility, χ, of human tissue using phase data. While brain imaging has been the most common application, other areas have also raised interest. For example, QSM of the articular cartilage of the knee has been suggested as a means to study the degeneration of this tissue. This would be of interest, as degeneration of articular cartilage is strongly related to the progression of osteoarthritis (OA). However, QSM of the knee is not straightforward, as the signal from fatty tissue complicates the reconstruction process due to its many frequency components. To avoid this issue, masking has been used to exclude fatty tissue from the reconstruction process. This is a relatively simple approach to a complicated problem, but, it might also be a source of bias in the susceptibility maps obtained. Another approach is the removal of chemical shift through chemical shift encoded imaging (CSEI) before QSM. The purpose of this work was to evaluate and compare the effects these approaches have on the estimated susceptibility values.

Materials and methods

Numerical phantoms were created based on two sets of MR images of knees, by defining various lean and fatty tissue compartments and assigning these literature susceptibility values. From these, phase images were simulated, which, in turn were used for QSM reconstruction. Comparisons were conducted between different background field removal techniques, and masking alternatives excluding: 1) no tissue, 2) bone marrow and 3) all fatty tissues from the reconstruction process. The performance of the different alternatives was evaluated by how well the ground truth was reproduced. Potential sources of error in the CSEI were also simulated.

The two approaches to handle signal from fatty tissue in the susceptibility calculation were also tested *in vivo*. Here, comparisons were made using the same background field removal techniques and masking alternatives as for the simulations.

Results

In the simulations, the ground truth was reproduced most reliably when no tissue was excluded from the reconstruction process, while masking of fatty tissue introduced a bias in the obtained susceptibility values. The size of this bias depended on the background field removal technique employed, how much of the fatty tissue that was excluded and the geometry of the knee evaluated.

Results obtained from *in vivo* data corresponded to results reported in earlier studies, and confirmed the simulation results of this study. However, both with and without CSEI, artefacts were seen when masking of fatty tissue was not performed. These were mitigated by exclusion of fatty tissue. The severity of these artefacts was greater without CSEI.

Conclusion

Exclusion of fatty tissue resulted in bias in the calculated susceptibility maps. Inclusion of fatty tissue in the reconstruction processes yielded more robust results between reconstruction techniques and geometry. However, in the *in vivo* results, the exclusion of fatty tissue from the reconstruction process mitigated artefacts stemming from imperfect CSEI.

Inclusion of fatty tissue in QSM reconstruction is advantageous, assuming that an accurate enough CSEI may be performed. If fatty tissue is excluded from QSM reconstruction, a suitable choice of background field removal technique may limit the bias caused.

Contents

1 Introduction

Osteoarthritis (OA) is a degenerative joint disorder, which has been estimated to affect up to 250 million people world wide [1]. Of these cases, 85% affect the knee, making this the most common site of the disease [2]. Though the severity varies, OA may cause great disruptions to everyday life as it is associated with both pain and reduced mobility of the joint. Little is known of the mechanisms causing these symptoms, but a number of factors which increase the risk of developing OA have been identified, including previous injury of the joint, obesity and higher age [1].

Currently, OA cannot be cured, and only limited treatment options are available. Generally, these treatments aim to reduce the symptoms of the disease rather than the causes, for example with pain management and walking aids [3]. As a last alternative, knee replacement surgery may be performed [4]. To find better treatment alternatives, it is important to gain a better understanding of the processes occurring during the early stages of OA.

An important tissue to study is the articular cartilage, as its degeneration is strongly associated with the progression of the disease. Although loss of cartilage is well known in late stage OA, macroscopic damage is preceded by microscopic changes already at an earlier stage [4]. In a healthy knee the articular cartilage is highly organized with a layered collagen structure [5]. This structure has been suggested to change in patients with OA. However, to monitor this effect *in vivo*, a non-invasive method to measure collagen structure is needed.

Because of its soft tissue contrast, a modality which might make it possible to study early changes in OA is magnetic resonance imaging (MRI). Especially, quantitative MRI-based techniques may be useful for this purpose. A number of such techniques have been suggested for extraction of information about the condition of cartilage. For example, T2-mapping and T1ρ-mapping has been suggested as means to detect disruptions of the collagen matrix structure [6]. T2-mapping, however, is complicated due to its angular dependency, while the use of T1ρ-mapping is limited by a high specific absorption rate (SAR). Another promising technique for detecting changes in the articular cartilage is quantitative susceptibility mapping (QSM), which aims to estimate the magnetic susceptibility of materials. In the articular cartilage, magnetic susceptibility anisotropy of collagen may be utilized to asses the organization of the collagen network [7]. In the current work, QSM is applied and evaluated.

Previous QSM studies of the knee have been able to detect the layered structure of the collagen network of the articular cartilage located between femur and tibia [8]. The susceptibility decreased going from the cartilage surface towards each bone, yielding profiles over the articular cartilage with the lowest susceptibility values close to either bone surface, and the highest in the middle. Furthermore, studies suggest that this contrast changes at the onset of cartilage degeneration due to disruption of the collagen network [6, 9], or in case of stress from long distance running [10]. This means that changes in the collagen structure may be possible to detect using QSM.

However, QSM in the knee is problematic due to the morphology of the knee and the presence of fatty tissue, as the chemical shift of the MRI signal from fatty tissue is a challenge for QSM reconstruction. The articular cartilage is located in close proximity to several volumes of fat, including bone marrow adipose tissue of the tibia, femur and patella, as well as subcutaneous fat, the infrapatellar fat pad and intermuscular fat. Earlier, this has been handled by excluding regions containing fatty tissue from the reconstruction process [8, 10–12]. While straightforward, this approach may introduce errors as the susceptibility of the excluded tissue might not be fully accounted for, and as background field removal may be challenging in regions close to the edges of the mask. Alternatively, chemical shift may be modelled using chemical shift encoded imaging [13, 14]. To what extent the choice of strategy affects the resulting susceptibility values has not been thoroughly investigated.

The purpose of this work was to use simulations and in vivo images to compare two different approaches to address fatty tissue in QSM of the articular cartilage of the knee: 1) excluding fatty tissue by masking and

2) correction of chemical shift using chemical shift encoded imaging.

2 Theory

2.1 Anatomy of the knee

The knee is one of the larger joints of the body, found where femur meets tibia and fibula, see fig. 1a(I, II and III). Here, several components have to work together in order to make movement of the joint possible, including ligaments, muscles, the menisci and the articular cartilage.

The distal end of femur, and the proximal end of tibia constitute the main contact point between the upper and lower part of the joint. Here, the femur ends in two rounded parts called condyles, and meets the end of tibia, called the tibial plateau [15]. Between these bones, the medial and lateral meniscus and the articular cartilage is located, see fig. 1a(IV and V). This cartilage covers the bone surfaces within the joint and consists of a matrix of collagen fibers, which holds a number of other components such as water, chondrocytes and glycosaminoglycans [4, 16].

In a healthy human knee, the articular cartilage has an ordered structure, where three distinct layers can be observed [17, 18]. These layers are called the deep zone, the middle zone and the superficial zone, and each one is characterized by the orientation of its collagen fibers [4]. In the deep zone, the collagen fibers have an orientation perpendicular to the cartilage surface, while collagen in the superficial zone has a parallel orientation. In the middle zone a larger distribution of orientation directions is present [7, 8, 17]. The orientation of the collagen fibers in the different layers is shown schematically in fig. 1(b).

Additionally, several fat depots are present in and around the joint. Most notably, the bone marrow of femur and tibia constitutes two such volumes, see fig. 1c(VI and VII). Bone marrow is also present in the patella, see fig. 1c(VIII). Furthermore, fatty tissue is also found in the infrapatellar fat pad and as subcutaneous fat, see fig. 1c(IX and X).

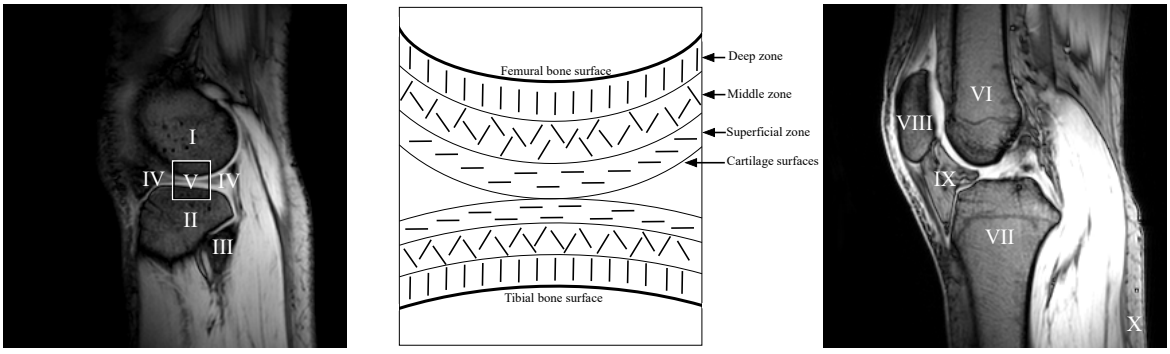

(a) (b) (c)

Figure 1: (a) Sagittal view a knee over the lateral femoral condyle of the knee with I: femur, II: tibia, III: fibula, IV: meniscus and V: articular cartilage. The area marked by the box in (a) is shown schematically in (b). Here, the orientation of the collagen molecules in each layer is shown. (c) Central sagittal view of the knee with the different fat depots, VI: bone marrow of femur, VII: bone marrow of tibia, VIII: patella, IX: the infrapatellar fat pad, and X: subcutaneous fat.

2.2 Magnetic susceptibility

Magnetic susceptibility, χ, is a property which describes the magnetization of a material subjected to an external magnetic field. The relationship between the magnetization (M) and the magnetic field strength (H) is expressed as

$$M = \chi H, \tag{1}$$

where M is a measure of the magnetic dipole moment per unit volume. In a material which is magnetised a field is created around the susceptibility source.

Human tissue is almost exclusively diamagnetic [19], but paramagnetic components can also be present in the body, resulting in a range of susceptiblity values [20]. The diamagnetic effect is always present, but only noticeable when not overshadowed by a paramagnetic effect [21].

Paramagnetism is only present when the atoms of the material has an unpaired electron. In such cases, the magnetic moment of the unpaired electron is not cancelled by that of another electron. If a material of this kind is subjected to an external magnetic field, magnetic moments will to a larger extent align with the external field. This results in a magnetization parallel to the external magnetic field, and thus an increase of the local field. Materials demonstrating this effect is referred to as paramagnetic and has a susceptibility larger than zero.

If there are no unpaired electrons, the magnetic moment of the electrons in each pair cancel, meaning that there will be no alignment with an external magnetic field. Instead, only the diamagnetic effect is observed. When an external field is applied, the field causes a shift in the motion of the electrons of the material. The shift, in turn, induces a weak magnetic field in the opposite direction of the applied field. Materials where only the diamagnetic effect is present are called diamagnetic. The susceptibility of such materials is negative and the local magnetic field will be lower compared to the applied external magnetic field [21].

2.3 Quantitative susceptibility mapping

QSM is a technique for calculating voxel-wise susceptibility values of materials using MRI phase data [7, 22]. This is possible as the local magnetic field affects the precession frequency, and thus the phase, of the magnetization vector. In QSM, phase images are used to evaluate the total magnetic field perturbation, ΔB, of the external field of the MRI scanner, B_0. This makes it possible to estimate the underlying susceptibility distribution [23]. A well known complication of the QSM reconstruction process is the underdetermination of the relationship between the magnetic field perturbation and the susceptibility distribution. This makes QSM noise-sensitive, and is the cause of so called streaking artefacts.

In order to perform these calculations, the data must be collected in a particular way and a number of post processing steps are required, see step 7-9 in fig. 2. In this section, the necessary image acquisition techniques and post processing steps will be discussed.

2.3.1 Image acquisition

To utilize the relationship between the perturbation of the external magnetic field and MRI phase data, image acquisition must be performed using a pulse sequence which does not erase effects caused by T2'-relaxation, making gradient recalled echo (GRE) sequences suitable [24].

In QSM, multi-echo GRE sequences, from which magnitude images, M_i, and phase images, ϕ, can be reconstructed, are commonly used. The collection of images using several echo times, TE, make it possible to evaluate the phase evolution over time, and identify an initial phase offset in the phase data, see below.

2.3.2 Estimation of the total field perturbation, ΔB, without chemical shift removal

In water-based materials, such as lean tissue, containing only one frequency component, the phase of the magnetization vector may be used to evaluate the perturbation of the external magnetic field through the relationship

$$\phi(TE) = \phi_0 - \gamma \Delta B TE. \tag{2}$$

Here, $\phi(TE)$ is the phase image collected at the echo time TE, ϕ_0 the phase at TE=0 and γ the gyromagnetic ratio. ΔB represents the magnetic field perturbation in the B_0 direction caused by the presence of the imaged

material, i.e. the relative difference between the magnetic field of the MRI-scanner with and without the imaged object placed in it. So, under "ideal" circumstances, knowing the phase of the MRI signal and ϕ_0, it would be possible to directly extract the field perturbation. In reality though, this is not possible for two reasons. First, the phase offset at TE = 0 must be determined. This is done by fitting the phase evolution of the signal, making it possible to extrapolate the phase offset at time zero. Secondly, the issue of phase wrapping must be resolved. This effect occurs when the range of phases of the magnetization vectors is larger than one revolution, i.e. [-π, π). If this is the case, the wrapping will present itself as a sudden increase or drop in intensity compared to adjacent voxels in areas where either of the phase limits is exceeded. In these cases, phase unwrapping (step 7, fig. 2) must be performed. This can be done using different methods, which aim to assign a correct multiple of 2π to the wrapped phase. From the unwrapped phase map, the field perturbation may be obtained from eq. (2).

2.3.3 Estimation of the total field perturbation, ΔB, with chemical shift removal

In fatty tissue, however, complications in evaluating field perturbation from the signal phase arises, as the signal phase is affected not only by the perturbation of the magnetic field, but also by the presence of several frequency components [25]. The reason for this is that the precession frequency of spins in water molecules differ from that of spins in fat molecules, causing a chemical shift in the signal from fat relative that of water. Furthermore, the precession frequency of spin in fat depends on its location in the molecule, giving the signal from fat several frequency components. These differences in signal behaviour mean that a more complex expression is needed in order to describe how the signal evolves over time when both water and fat is involved. From one voxel containing both water and fat, the complex MRI signal, $S(TE_n)$, collected at the n-th echo time, TE_n, may be described using the following equation [13, 26, 27]:

$$S(TE_n) = \left(\rho_W + \rho_F \sum_{m=1}^{M} \alpha_m e^{i2\pi\Delta f_m TE_n}\right) e^{i2\pi\hat{\psi}TE_n}. \tag{3}$$

In this equation, ρ_W and ρ_F are the signal amplitudes from water and fat at $TE = 0$ respectively, α_m the amplitude of peak m in the fat spectrum relative to the sum of their amplitudes, and Δf_m the chemical shift of peak m relative to water. The echo time at which the data is collected is given by TE_n, and $\hat{\psi}$ represents the combined effect of the transverse relaxation time of the tissue in the voxel, T2*, and the perturbation of the external magnetic field in the voxel, ΔB, as follows:

$$\hat{\psi} = \Delta B + i\frac{TE_n}{T2^*}, \tag{4}$$

If image data is collected using bipolar gradients and interleaved echo times, phase effects from e.g. gradient delays and frequency dependency of the coil needs to be corrected. This may be done by including the correction terms [28]

$$e^{(-1)^n i\theta_{bip}} e^{I(n)i\theta_{int}}, \tag{5}$$

in eq. (3). Here, θ_{bip} and θ_{int} represent the errors introduced by these effects. I is a matrix defined as

$$I = [1, 1, -1, -1, 1, 1...] \tag{6}$$

From eq. (3) and eq. (5), the phase contributions caused by field perturbations and chemical shift may be separated using chemical shift encoded imaging (CSEI). This is done using an iterative process starting with a model where α_m and Δf_m are known a priori and using an initial guess for $\hat{\psi}$. Estimations of ρ_W and ρ_F and $\hat{\psi}$ are then iteratively updated until a minimum is found. Using this approach, a map of the total field perturbation may be obtained. This map of the total magnetic field perturbation may then be used as input in the background field removal step in the QSM pipline described below (step 8, fig. 2).

2.3.4 Background field removal

The total field perturbation estimated does not purely consist of a field induced by susceptibility-differences between the materials within the object. Instead, the total field perturbation (ΔB) may be described as consisting of two components, the local magnetic field and the background field, as follows:

$$\Delta B = \Delta B_{local} + \Delta B_{background}. \tag{7}$$

Here, ΔB_{local} is the field generated by susceptibility sources within the object, and $\Delta B_{background}$ the field generated by the susceptibility difference between the object and the background. Additionally, imperfect shimming affects the background field. In order to asses the susceptibility values within the object, the background field must be removed (step 8, fig. 2). Background field removal is performed within an area defined by a mask. This mask often covers the whole object of interest, but it is also possible to exclude parts of the object. The area covered by the mask will be referred to as the region of interest (ROI).

A number of approaches for removal of the background field have been suggested and implemented. Two commonly used methods are Projection onto Dipole Fields (PDF) [29], and the Laplacian boundary value method (LBV) [30]. Both of these assume a harmonic background field and a non-harmonic local field as their basis for separation.

The PDF technique is based on the observation that the magnetic field from a dipole within and outside of the ROI are approximately orthogonal. This is seen as the inner product between the two fields is close to zero. Knowing the total field within the ROI, a separation of the local field and the background field is possible through the projection of the total field onto the plane spanned by the background field.

In LBV, the separation is performed using Laplace's equation to describe the background field within the ROI in combination with an approximation of the background field at the boundary of the ROI. While the background field is not known, it is approximated to be equal to the total field, using the assumption that the background field is much larger than the local field. By solving this equation, the local field may be separated from the background field.

2.3.5 Dipole field inversion

Once ΔB_{local} has been extracted, the susceptibility distribution of the material in the ROI may be estimated. In order to do this, a relation between susceptibility and field perturbation is needed. Such a relation can be established using the dipole field created by each susceptibility source when magnetised. The field perturbation may then be expressed as a convolution between a dipole kernel and the susceptibility distribution:

$$\Delta B(\bar{r})_{local} = B_0(d(\bar{r}) \circledast \chi(\bar{r})). \tag{8}$$

Here, $\chi(\bar{r})$ denotes the susceptibility at a coordinate position $\bar{r}$, B_0 the strength of the external magnetic field, and $d(\bar{r})$ the unit dipole kernel, which in the spatial domain is given by the equation

$$d(\bar{r}) = \frac{1}{4\pi}\frac{3\cos^2(\theta) - 1}{|\bar{r}|^3}, \tag{9}$$

with θ as the angle between $\bar{r}$ and the direction of B_0. This convolution in the spatial domain corresponds to a multiplication in Fourier space, which is written as

$$\Delta B(\bar{k})_{local} = B_0 \left(D(\bar{k}) \cdot X(\bar{k})\right), \tag{10}$$

with $X(\bar{k})$ being the Fourier transform of the susceptibility distribution at a coordinate position $\bar{k}$. The Fourier transform of the dipole kernel, $D(\bar{k})$, is given by the equation

$$D(k) = \frac{1}{3} - \frac{\bar{k}_z^2}{\bar{k}^2}, \quad \bar{k} \neq 0. \tag{11}$$

Here, $\bar{k}_z$ is the component of $\bar{k}$ parallel to B_0.

If the local perturbation of the external field is known, this expression may be used to calculate the susceptibility map as a deconvolution of the local magnetic field with the dipole kernel in the spatial domain, or correspondingly, as a division in the Fourier space. The susceptibility map in the spatial domain is then given by [31]:

$$\chi(\bar{r}) = \frac{1}{B_0}\mathscr{F}^{-1}\left(\frac{\Delta B_{local}(\bar{k})}{D(\bar{k})}\right). \tag{12}$$

This operation is not unproblematic, because of how the dipole kernel is defined. As is seen from eq. (11), the dipole kernel will have the value 0 where the ratio between $\bar{k}$ and $\bar{k}_z$ is $\frac{\bar{k}^2}{\bar{k}_z^2} = \frac{1}{3}$. In the fourier domain, these values occur along the surfaces of two cones extending outwards at an angle of 54.7° from the main field, and around these surfaces, the values of the dipole kernel are approaching zero. This yields a problem without a unique solution, thus complicating the evaluation of the susceptibility values from the local magnetic field perturbation. Furthermore, the low values around the surface of the cone amplify noise in the local field map, resulting in streaking artefacts.

Several approaches have been suggested to address this problem. For example, performing data collection with several orientations of an object (COSMOS) [32], or truncated k-space division (TKD) [33, 34]. Another approach is the use of morphological data to increase the information of the object. An implementation of this is called Morphology Enabled Dipole Inversion (MEDI) [35]. This implementation was used in the current project.

In MEDI, it is assumed that edges in the susceptibility map should correspond to edges in the magnitude image. In this way, streaking artefacts may be identified, as there generally are no corresponding edges in the magnitude image to match them. Using this, the number of voxels belonging to edges in only the susceptibility map can be minimized. This is done through the extraction of an edge mask, M_e, using the gradients in the signal intensity of the magnitude image as a base. This mask is given as a matrix, where regions with small or no gradients are assigned the value one and those were gradients are detected are set to zero. Similarly, gradients in the susceptibility map is obtained by applying the gradient operator, ∇, to it. With this, the function to be minimized is expressed as

$$E(\chi, \lambda) \equiv ||M_e \nabla\chi||_1 \ + \lambda \ (||W(\mathscr{F}^{-1}(DX)) - \Delta B_{local}||_2^2 - \epsilon). \tag{13}$$

Here, the second term forms a constraint which keeps the difference between the measured field perturbation, ΔB_{local}, and the estimation of the local field perturbation assuming a certain susceptibility distribution, $\mathscr{F}^{-1}(DX)$, as low as possible, considering the accuracy the data collection is performed with. This accuracy is given by the noise level, ϵ, which is estimated at the same time as the total field perturbation, and is inversely proportional to the squared image intensity [36]. W is a weighting matrix needed as the phase noise of the image is not uniform, and λ a Lagrange multiplier.

The function E(χ, λ), is then minimized by iteratively updating a susceptibility distribution starting from an initial guess. Here, each update aims to result in a smaller value of E(χ, λ). Mismatches between the susceptibility map and magnitude image will increase the value of E(χ, λ), while the absence of such mismatches will yield a smaller value. This, in turn, means that the minimization process gives a susceptibility distribution where edges which do not match the magnitude image are penalized. It is important to note, that the choice of λ affects the impact of the magnitude image on the final susceptibility map. A low value of λ results in a high impact of the magnitude image, while a high value does the opposite [37].

2.3.6 Anisotropy of magnetic susceptibility

The local magnetic field perturbation, ΔB_{local}, caused by an object might depend on its orientation relative to the external magnetic field. This may be attributed to one of two effects: 1) susceptibility anisotropy of the molecules in the object or 2) the shape of the imaged object [21, 38].

In the first case, anisotropic susceptibility of molecules in a material affect the local magnetic field differently depending on their orientation towards the external magnetic field. In ordered materials, this susceptibility anisotropy of the molecules can be seen to cause orientation dependence on QSM contrast [7]. This is for example the case in articular cartilage, where collagen fibrils have an anisotropic magnetic susceptibility, yielding different contrast between regions with different collagen fibril orientation [7, 8, 38].

In the second case, spatial constraints on a material with an isotropic susceptibility yields an orientation dependent perturbation of the external magnetic field caused by spin interaction within the object [21]. The second effect is seen when other techniques, such as T2*-mapping and susceptibility weighted imaging (SWI), are employed. By using QSM, however, this effect may be avoided [39].

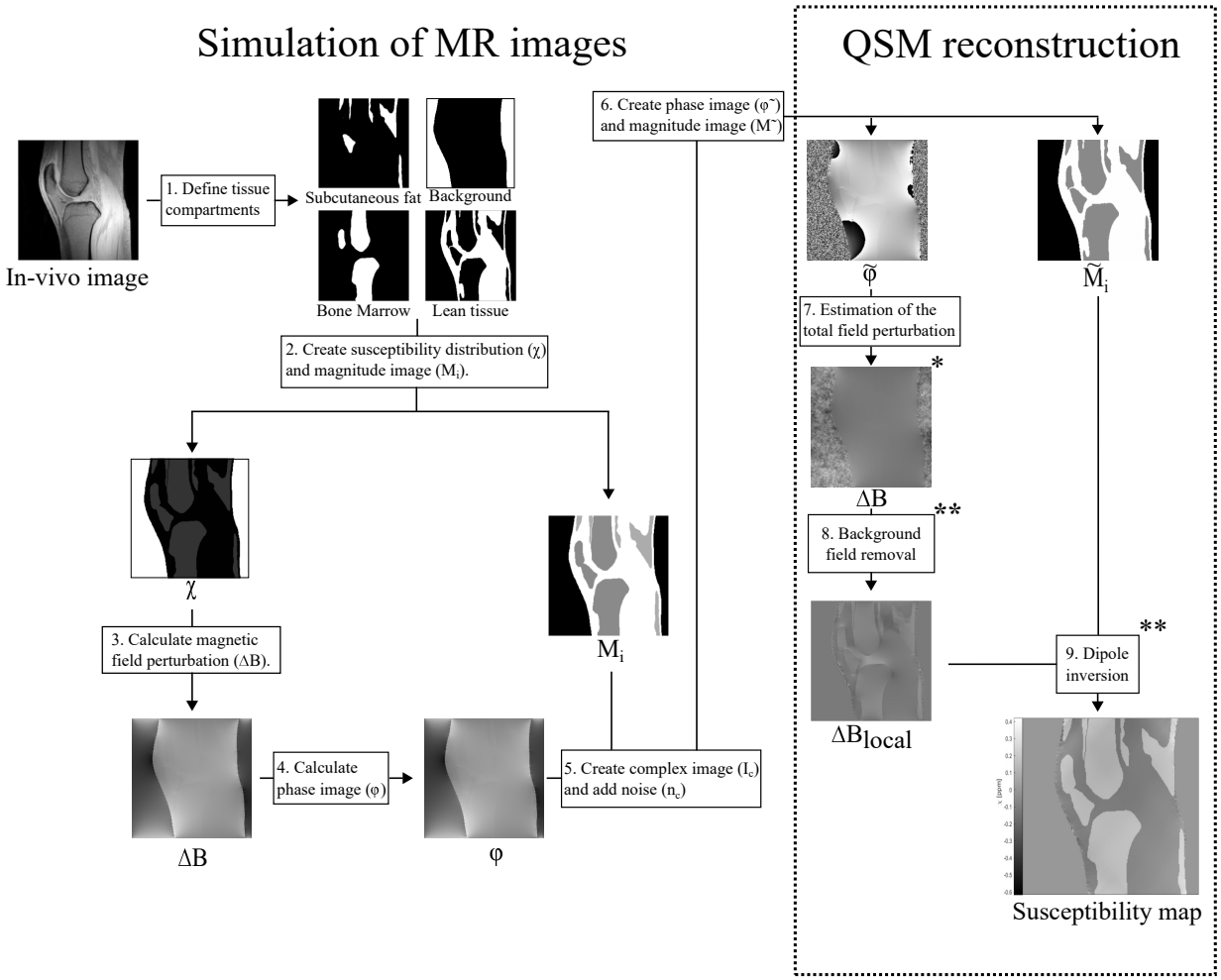

Figure 2: To the left: The steps included in the simulation process moving from *in vivo* images to simulated phase and magnitude images. To the right: The steps used for the QSM reconstruction of susceptibility maps. These steps were used for both the simulated and *in vivo* images. * marks the place where potential sources of error in CSEI were simulated, and ** the places where masking of fatty tissue was performed.

3 Materials and methods

The aim of the current project is to gain a better understanding of how different approaches of handling the signal from fatty tissue affect the calculated susceptibility values in the articular cartilage. The two approaches studied are: 1) exclusion of fatty tissue from the reconstruction steps by masking, and 2) modeling the chemical shift in the estimation of ΔB through CSEI.

The simulations were used to investigate if exclusion of fatty tissue results in biased QSM reconstruction, focusing on two effects. First, whether or not the susceptibility of the excluded fatty tissue is accounted for in the background field removal step, or if the exclusion of this tissue results in a loss of information. Secondly, if introducing edges close to the articular cartilage affect the estimated susceptibility values. Two potential sources of error in the second approach were also simulated and evaluated: extreme values and residual bias in the ΔB map.

Next, *in vivo* images were evaluated to confirm the simulation results and to evaluate the use of CSEI.

All simulations and data processing was performed using Matlab (MATLAB R2022a, TheMathworks, Natick,MA).

3.1 Image acquisition

Image data from two knee-healthy research subjects was used in this work. The data sets were part of an ongoing research project with permission from the ethics review authority and after written informed consent. Magnitude and phase images were collected using a Philips 7T scanner. Each participant was scanned with a multi-echo GRE with 8 TEs. The sequence was scanned twice with interleaved echo timed so that $TE_1/\Delta TE = 1.2$ ms/1.2 ms for the first scan, and $TE_1/\Delta TE = 1.8$ ms/1.2 ms for the second, creating an effective ΔTE of 0.6 ms. In both sequences, TR = 30 ms, matrix size = 256x256x37 and voxel size = 0.58x0.58x3 mm^3. Additionally, the B_0-map from Philips mDixon algorithm was used as the initial guess in CSEI.

3.2 Simulations

3.2.1 Numerical phantom

From each of the two *in vivo* data sets, numerical phantoms were created based on the magnitude images and a fat fraction map calculated using CSEI. From this image data, four compartments were defined through thresholding: air, bone marrow, subcutaneous fat and lean tissue (step 1, fig. 2). Image data from two participants was used in order to study how variations in geometry and the amount of subcutaneous fat affect the results. The matrix and voxel sizes of the numerical phantoms matched those of the image data.

By assigning each compartment a literature susceptibility value [8, 40, 41], a susceptibility map was created (step 2, fig. 2). Similarly, a magnitude image was created using the same compartments, but with signal values based on those of the *in vivo* knee images (step 2, fig. 2). The values assigned to each compartment in the susceptibility distribution and the magnitude image are listed in table 1.

Table 1: Values assigned to the compartments in the simulated susceptibility distribution and magnitude image using a susceptibility of 0 ppm for water as a reference.

Compartment	Susceptibility [ppm]	Magnitude image signal value
Background	9	0
Lean tissue	-0.18	740
Bone marrow	0.45	400
Subcutaneous fat	0.45	500

The susceptibility map was padded with zeros in order to avoid circular convolution affecting the characteristics of the simulated background field [25,41], before calculating the total magnetic field perturbation, ΔB, using eq. (10) (step 3, fig. 2). Here, the magnetic field strength of the external field, B_0 was given the value 7 T. The total magnetic field perturbation is here expressed in units of rad/echo, to follow the standard used in the MEDI software package.

A phase map, ϕ was created using the relationship in eq. (2) with $\phi_0 = 0$ and TE = 1.2 ms (step 4,

fig. 2). Next, a complex image, I_c, was created using the simulated phase and magnitude images (step 5, fig. 2). To this, complex Gaussian noise, n_c, with mean 0 and standard deviation 10^{-8} was added as follows:

$$I_c = M_i * e^{(i\phi)} + n_c. \tag{14}$$

Noise was needed in the susceptibility calculations, but was kept low in order to not influence the results more than necessary, as the effects of masking of fatty tissue was to be evaluated rather than that of noise.

From the complex image, new magnitude- and phase images $\tilde{M}_i$ and $\tilde{\phi}$, were defined as the absolute value and the phase of the complex image, respectively (step 6, fig. 2). The resulting magnitude and phase images were then processed with the reconstruction steps described in section 4.3: Estimation of the total field and phase unwrapping, background field removal and dipole inversion. (step 7-9, fig. 2). Phase unwrapping was performed using graph cuts [42], background field removal using PDF [29, 43] and LBV [30], and dipole inversion using MEDI [35], all of which were implemented in the MEDI software package [35, 37, 44, 45].

Background field removal was performed using the settings: tol = 0.05, depth = -1 and peel = 0 for LBV. PDF was performed using default values. For dipole inversion, $\lambda = 1000$ was used. The susceptibility values were not referenced, and the SMV setting was not used.

No chemical shift was included in the simulations, meaning that CSEI was not needed in the reconstruction.

3.2.2 The effects of excluding fatty tissue

In order to evaluate the effect of excluding fatty tissue from the QSM reconstruction, background field removal and dipole inversion was performed using three different masking alternatives: 1) excluding no tissue, 2) excluding bone marrow and 3) excluding all fatty tissues, see fig. 3. For each masking alternative two background field removal techniques, PDF and LBV, were used.

Additionally, a susceptibility map was calculated with mismatching masking alternatives between background field removal and dipole inversion. This was done by performing dipole inversion with all fatty tissues excluded based on the local fields obtained with no tissue excluded and all fatty tissues excluded. Thus, the effect of not matching masks between the background field removal and dipole inversions steps was investigated.

The results were evaluated by comparing the local field maps and susceptibility maps obtained using the different masking alternatives. Furthermore, profiles over the area where the articular cartilage would be situated in the susceptibility maps were extracted. This was done within a square region, where the mean and standard deviation of the values within each row of voxels parallel to the bone surfaces were extracted. The mean and standard deviation of each such row was plotted as a function of its distance from the femoral surface. As the susceptibility values obtained are relative, the values were shifted in order to simplify the comparison between them by assigning the mid-point between the femur and tibia a zero susceptibility. All points within a profile were shifted equally. A slice through the medial femoral condyle was chosen for analysis. The area over which the profiles were evaluated for each knee is shown in fig. 4.

3.2.3 Potential sources of error in CSEI

So far, no chemical shift was added in the simulations and the phase maps used thus corresponded to a situation following perfect CSEI. Using the same numerical phantoms, simulations of potential sources of error in CSEI were made to visualize how such errors would affect the following susceptibility calculations. Two potential errors were simulated: 1) extreme values in the estimated total field map and 2) residual shifts in the estimated total field map. Both of these were simulated by adding phase shifts to the total field map, yielding a phase not completely explained by the underlying susceptibility distribution. *In vivo*, extreme values may occur either if the iterative estimation of the total field perturbation stops in a local minimum

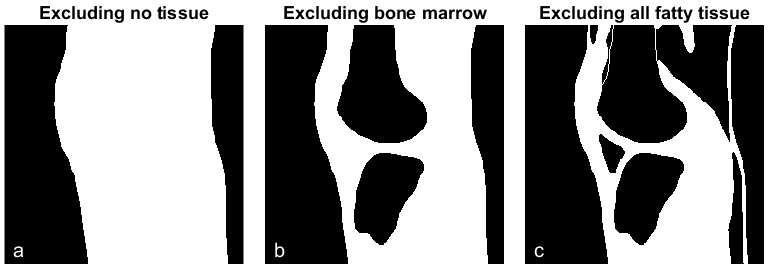

Figure 3: The three masking alternatives, (a) excluding no tissue, (b) excluding bone marrow and (c) excluding all fatty tissues, that were used for simulations.

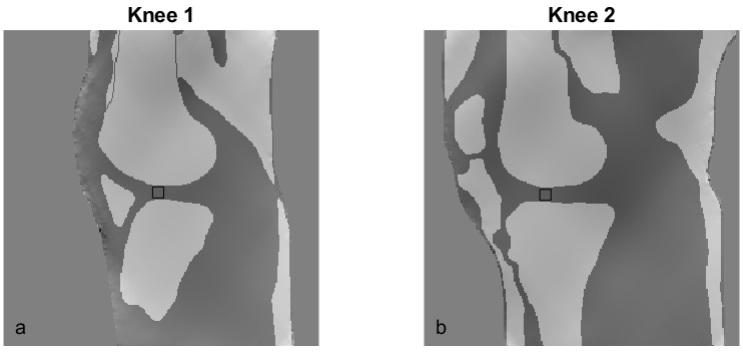

Figure 4: The slices of (a) knee 1 and (b) knee 2 where the profiles were evaluated. The black boxes shows the area in which the profiles were studied.

or if no satisfactory solution is found before termination of the iterative process, while residual shifts may occur if the model of the chemical shift is inaccurate.

Extreme values were simulated by increasing the values of some pixels in the total field map, marked with (*) in fig. 2. The location and size of the values in these pixels, set to 40 rad/echo, was based on preliminary results from *in vivo* data, see fig. 5(a, c). An imperfect removal of the chemical shift was simulated by changing the values of the bone marrow compartment in the total field map, marked with (*) in fig. 2. Three different residual chemical shifts were simulated: -0.23 rad/echo, 0.11 rad/echo and 0.023 rad/echo. These shifts corresponded to an offset of -0.1 ppm, 0.05 ppm and 0.01 ppm relative to the larmor frequency. The area where this additional shift was added is shown in fig. 5(b). The size of the shifts were chosen to imitate the variation of the chemical shift which may occur due to bulk magnetic susceptibility effects present in fatty tissue [46].

Additionally, a residual chemical shift only located at the edges of the bone marrow compartment (fig. 5(d)), approximately corresponding to the cortical bone, was simulated. This was done in the same way as with the whole bone marrow compartment. In this case, the residual chemical shift used was 0.05 ppm.

Following this, susceptibility maps were reconstructed using both PDF and LBV for background field removal for background field removal followed by MEDI for the dipole inversion.

3.3 Analysis of in vivo images

Finally, the approaches for addressing signal from fatty tissue were compared when applied to *in vivo* data. First, QSM was performed with the three masking alternatives with and without CSEI. This was done to evaluate the necessity of removing the chemical shift before the susceptibility calculations. The use of CSEI

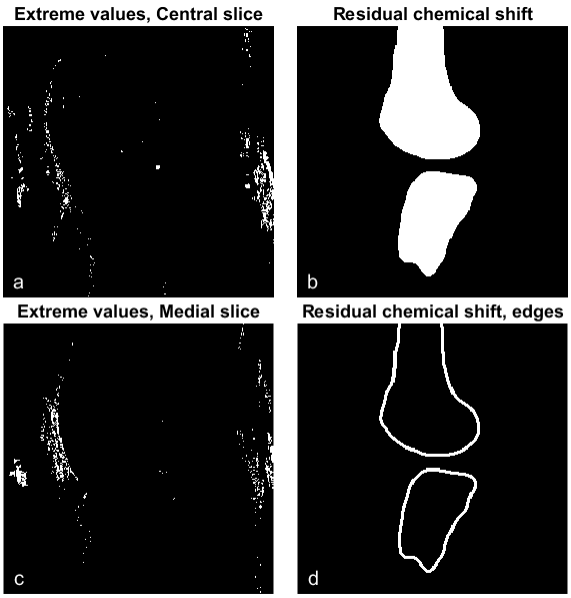

Figure 5: The regions where values were changed in the estimated total field map in the simulations of extreme values (a, c), and residual chemical shifts (b, d).

yielded maps representing the frequency offset relative to the larmor frequency in each voxel, see eq. (3). This frequency offset was converted to a map of the total magnetic field perturbation, which was then used as input in the background field removal step. The conversion from frequency map, Δf, to total field perturbation, ΔB, was performed using the conversion factor $2\pi\Delta TE$, with ΔTE=0.6 ms.

For the reconstruction without CSEI, fitting for extrapolation of the phase offset was performed using a function for complex fitting implemented in the MEDI software package [36, 47, 48].

Additionally, QSM was performed following CSEI using each of the three masking alternatives, and the two background field removal techniques. Here, all settings were kept the same as in the simulations, except for λ, which was set to 200 in the dipole inversion step. In the susceptibility maps obtained, profiles were extracted in the same slice and position as in the simulations.

4 Results

4.1 Simulations

4.1.1 The effects of excluding fatty tissue

The choice of masking alternative affected the local field obtained after background field removal, see fig. 6. In the region between femur and tibia (pointed out by black arrows in fig. 6(a, b, d, e)) a distinctly higher local magnetic field was seen when no tissue was excluded, see fig. 6(a, d), compared to when bone marrow or all fatty tissue was excluded, see fig. 6(b, e, c, f). Similarly, differences were seen around the infrapatellar fat pad when the local field obtained with all fatty tissues excluded to was compared the other two masking alternatives, pointed out by white arrows in fig. 6(b, c, e, f).

Performing QSM with mismatching masks in the background field and dipole inversion steps gave distinct differences in the resulting susceptibility maps. When the masks did not match, a larger inhomogeneity was seen around the depots of fatty tissue, see fig. 7.

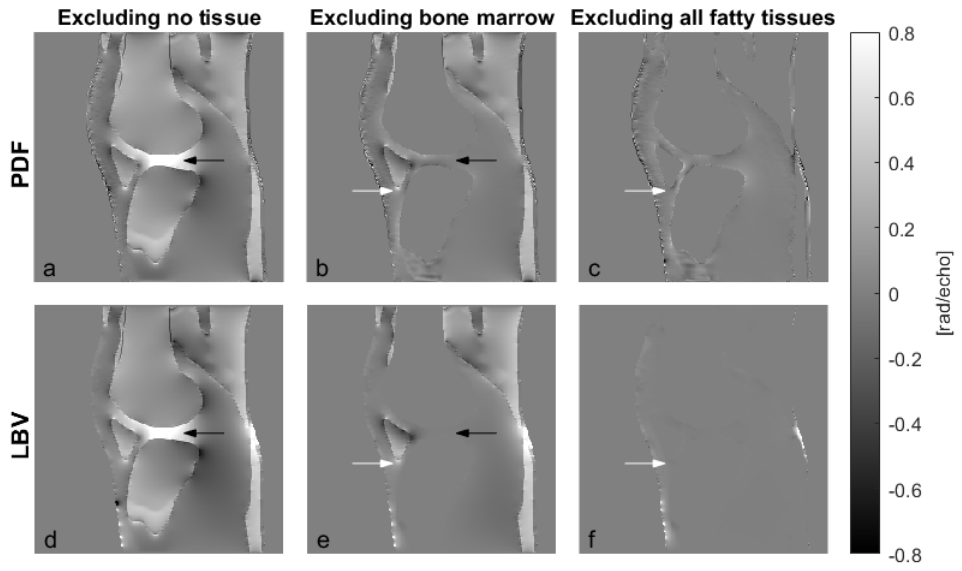

Figure 6: Local field calculated when (a, d) no tissue, (b, e) bone marrow and (c, f) all fatty tissue was excluded from the mask applied before background field removal. Background field removal was performed using PDF (a-c) and LBV (d-f) for comparison. The local field in the cartilage area is seen to be higher when bone marrow is not excluded. Differences when bone marrow was included and excluded are pointed out by black arrows, and differences when subcutaneous fat was included and excluded are pointed out by white arrows.

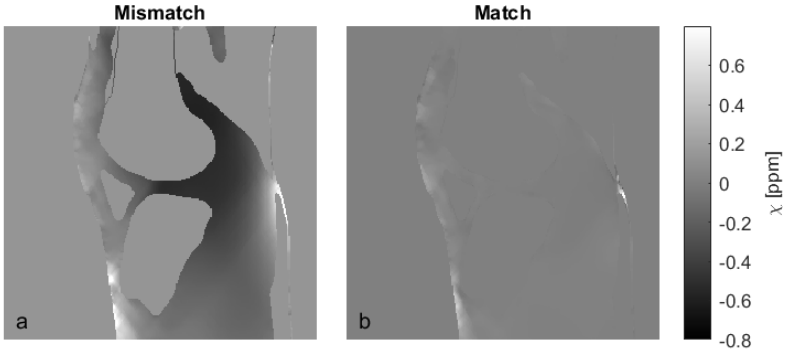

Figure 7: Susceptibility maps obtained with (a) a mismatch and (b) match between masking alternatives between background field removal and dipole inversion. Here, the mask excluding no tissue was used for background field removal for (a), and the mask excluding all fatty tissues for (b). In both cases, the mask excluding all fatty tissues were used for dipole inversion.

Both the choice of masking alternative and background field removal technique affected the susceptibility maps calculated, see fig. 8. With no tissue excluded, the susceptibility map obtained using PDF was relatively homogeneous, but with some irregularities which are seen at the front of the leg, pointed out by the black arrow in fig. 8(a). For LBV, these effects were not seen, but instead, an increase in the calculated susceptibility values which did not stem from the simulated susceptibility were seen in the front of the knee and the fold of the knee, marked by the black arrows in fig. 8(d). With the removal of fatty tissue from the reconstruction process, new errors were introduced. This is seen for both PDF (fig. 8(b, c)) and LBV (fig. 8(e, f)), but with more obvious effects for PDF.

Generally, the most homogeneous results were obtained when no tissue was excluded from the reconstruction

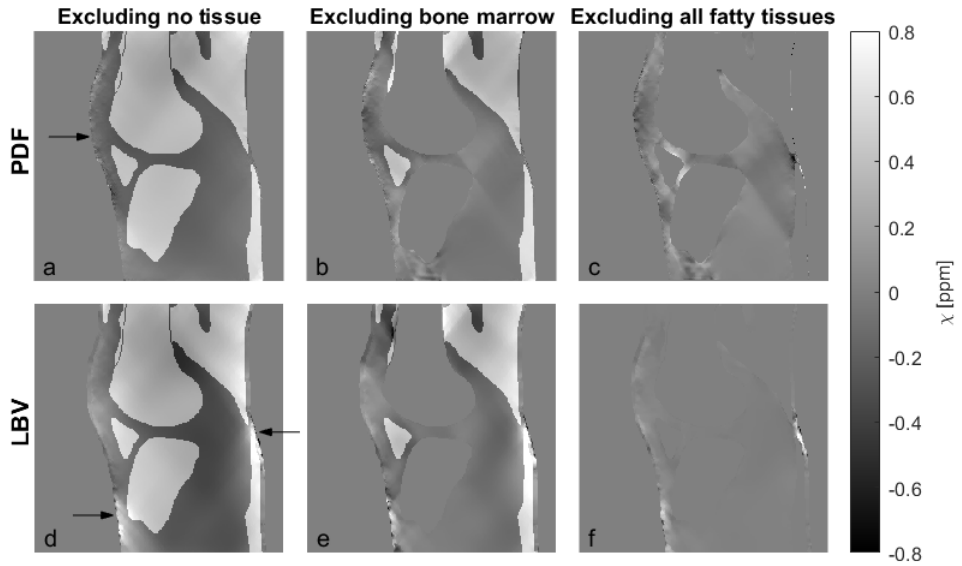

Figure 8: Susceptibility maps obtained when (a, d) no tissue, (b, e) bone marrow, and (c, f) all fatty tissue was excluded from the masks applied before the background field removal and dipole inversion steps. Background field removal was performed using PDF (a-c) and LBV (d-f) for comparison. Regions where artefacts are present in (a, d) are pointed out by black arrows.

for both knees and background field removal techniques, see fig. 9. Comparing the results of PDF and LBV, masking of fatty tissue introduced less errors when LBV was used than PDF.

Using PDF, the extracted profiles were more homogeneous when no tissue was excluded for both of the knee simulations, see fig. 9 (a, b). The two other masking alternatives, excluding all fatty tissue and excluding bone marrow yielded less homogeneous profiles over the cartilage area and a higher standard deviation within the rows.

Using LBV, the profiles obtained when no tissue was excluded showed similar results between the two knees, see fig. 9 (c, d). These results were comparable to those of PDF with the same masking alternative. However, for the two masking alternatives, excluding bone marrow or all fatty tissue, results varied between the two knees. Here, more homogeneous results were seen in the first knee compared to the second.

4.1.2 Potential sources of error in CSEI

The simulations of extreme values in the phase map showed that these might cause streaking artefacts in the reconstructed susceptibility maps, especially when groups of extreme values were present. In the case of single extreme values, the effects were not as severe, but still observable. The resulting susceptibility maps are shown in fig. 10.

A residual chemical shift in the phase map also caused streaking artefacts in the reconstructed susceptibility maps, both when it was simulated in the whole bone marrow compartment and when it was simulated in the edges of the same compartment. These streaking artefacts followed a similar pattern in both cases, see fig. 11. The severity of the artefacts depended on the size of the residual shift. For both -0.1 ppm and 0.05 ppm , artefacts were visible, even though those of 0.05 ppm were smaller than those of -0.1 ppm, see fig. 11(a, b, e, f). In the case of a residual shift of 0.01 ppm however, the artefacts were barely visible, see fig. 11(c, g).

It was also seen, that the sign of the residual chemical shift affects the resulting streaking artefacts. Comparing the resulting artefacts in the same area of the -0.1 ppm-shift and the 0.05 ppm-shift, the streaking

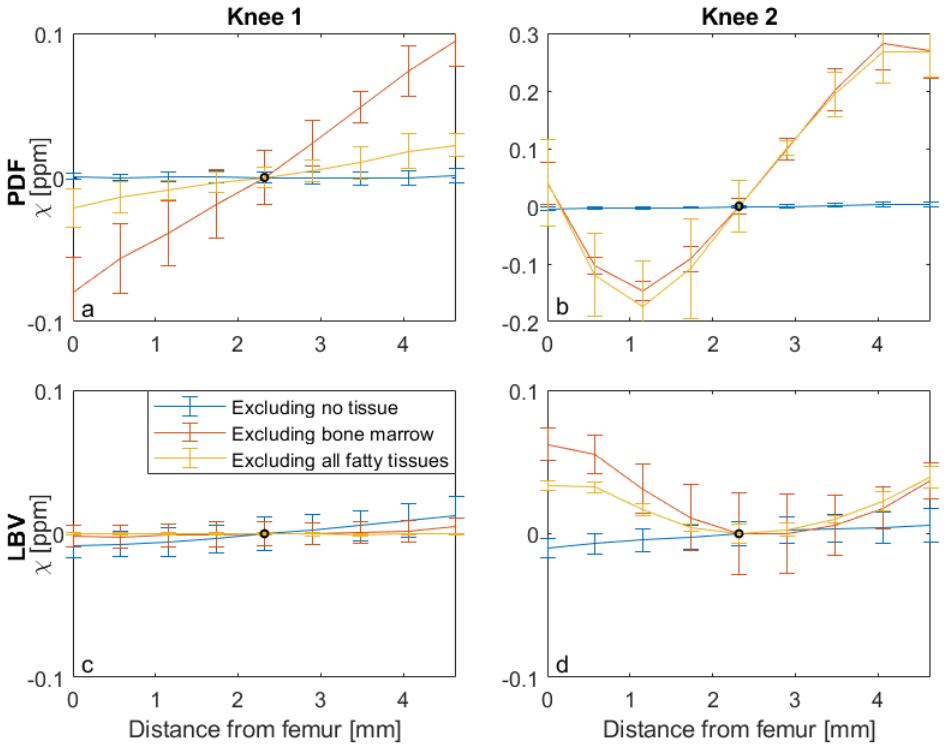

Figure 9: Profiles of the susceptibility values in the area between the femur and the tibia of knee 1 (a, c) and knee 2 (b, d) when the background field was removed using PDF (a, b) and LBV (c, d). The middle point between femur and tibia, which was assigned a zero susceptibility, is marked with a black circle. The expected flat profile was reproduced most reliably when no tissue was excluded from the reconstruction. Observe, that the results in (b) are presented using a larger y-scale than the others in order to show the whole profile for all masking alternatives.

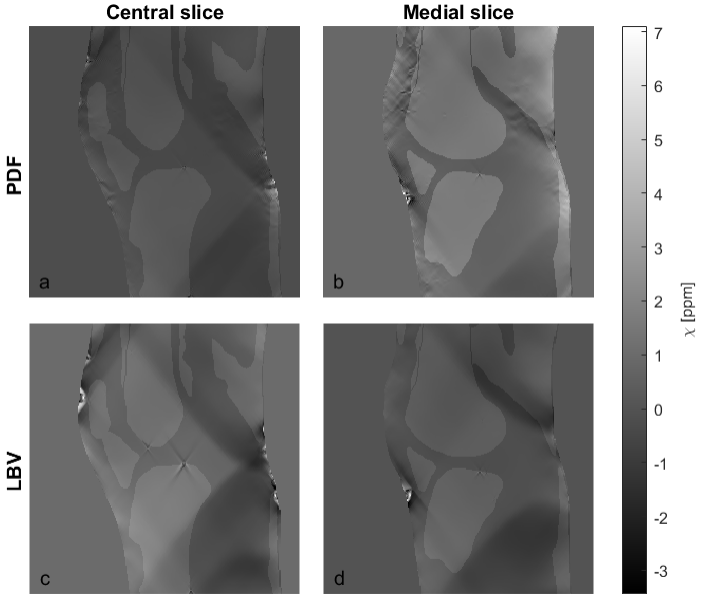

Figure 10: Susceptibility maps obtained after simulating extreme values in the estimated total field map. The results are shown in a central (a, c) and a medial slice (b, d) of the knee for the different background field removal techniques PDF (a, b) and LBV (c, d).

artefacts have opposing signs.

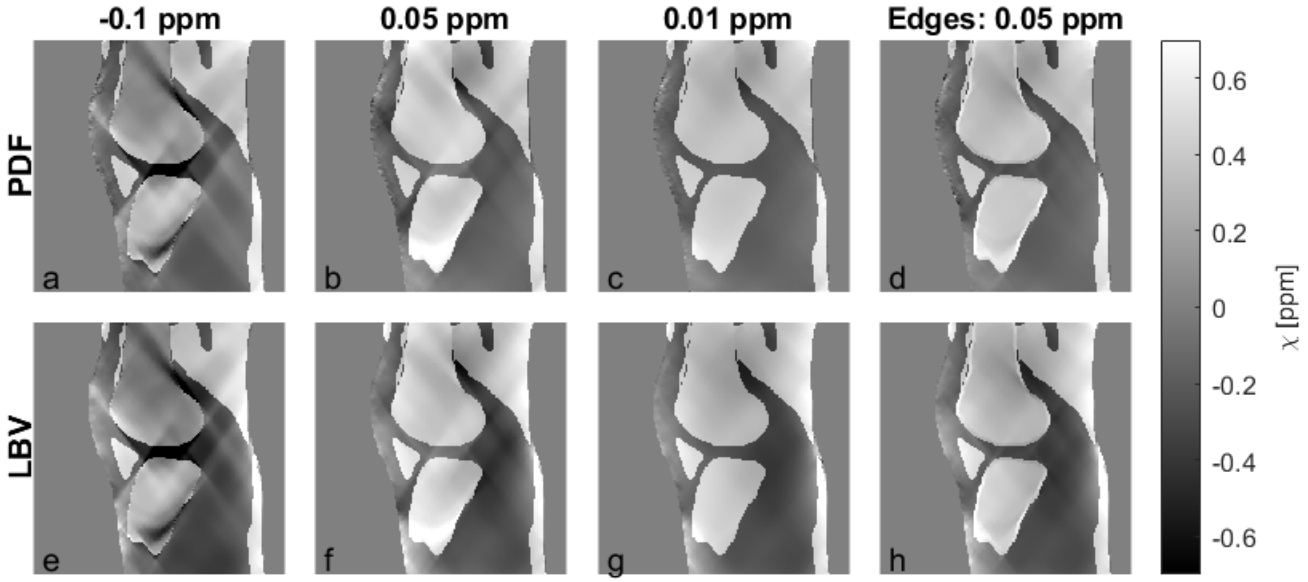

Figure 11: Susceptibility maps obtained after simulating residual chemical shift of (a, e) -0.1 ppm, (b, f) 0.05 ppm and (c, g) 0.01 ppm in the whole bone marrow compartment in the estimated total field map, as well as (d, h) a residual shift of 0.05 ppm in the edges of the bone marrow compartment only. Streaking artefacts are seen for all residual shifts except for 0.01 ppm. The severity of these increase with the size of the chemical shift.

4.2 Analysis of in vivo images

Streaking artefacts were seen both with and without the use of CSEI, but the severity of these artefacts was greater when no CSEI had been performed, see fig. 12. Comparing the results of masking fatty tissue with (fig. 12(a-c)) and without (fig. 12(d-f)) CSEI, masking of fatty tissue decreased the streaking artefacts seen in both cases.

When QSM was performed following CSEI, the results obtained for knee 1 showed streaking artefacts, pointed out by black and white arrows in fig. 13(a, d), when no tissue was excluded. These artefacts decreased or disappeared when fatty tissue was excluded from the reconstruction process. The areas where these artefacts would be located are pointed out by black and white arrows in fig. 13(b, c, e, f). The susceptibility maps of the articular cartilage is also seen in fig. 14, overlaid on a magnitude image. The results obtained from knee 2 showed similar results, where streaking artefacts were reduced by the exclusion of fatty tissue, see fig. 15. However, in the susceptibility map obtained using PDF and excluding bone marrow, see fig. 15(b), an artefact was seen over the articular cartilage that was not seen in any of the other susceptibility maps.

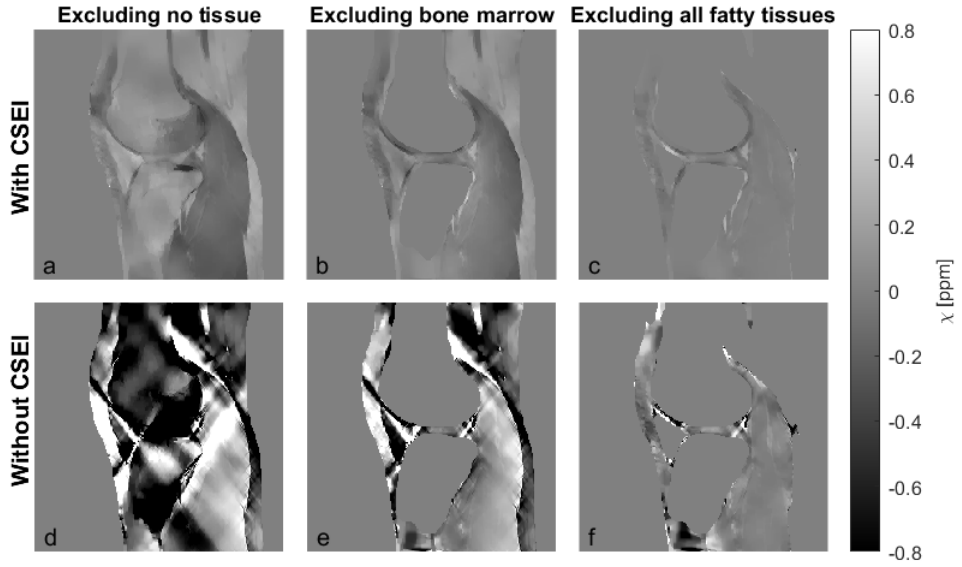

Figure 12: Susceptibility maps obtained when (a, d) no tissue, (b, e) bone marrow and (c, f) all fatty tissue was excluded from the masks applied before the background field removal and dipole inversion steps. Results obtained with CSEI are shown in (a-c), while results without CSEI are shown in (d-f). The artefacts seen were more severe without CSEI.

In the first knee, the profiles over the articular cartilage showed an increase in susceptibility values going from the deep zone to the superficial zone of either bone, see fig. 16 (a, c). This was seen for all three masking alternatives and both background field removal techniques, with slight variations.

In the second knee, the same shape was seen when no masking of fatty tissue had been performed, see fig. 16(b, d). Here, larger standard deviation was seen within rows compared to knee 1. For the other masking alternatives, the results differed between background field removal techniques. With LBV, similar shapes were seen for all masking alternatives, but with an offset close to the femoral surface in the masking alternatives where bone marrow or all fatty tissues were excluded. With PDF, on the other hand, distinct differences between all three masking alternatives were seen. Here, large susceptibility difference were seen, especially when bone marrow was masked.

Figure 13: Susceptibility maps obtained from *in vivo* data of knee 1 with chemical shift removal when (a, d) no tissue, (b, e) bone marrow and (c, f) all fatty tissue was excluded from the masks applied before the background field removal and dipole inversion steps. The results obtained using PDF for background field removal are shown in (a-c) and those using LBV in (d-f). Streaking artefacts were seen when fatty tissue was not excluded from the reconstruction. These were reduced by exclusion of fatty tissue. Examples of such artefacts are marked by black and white arrows.

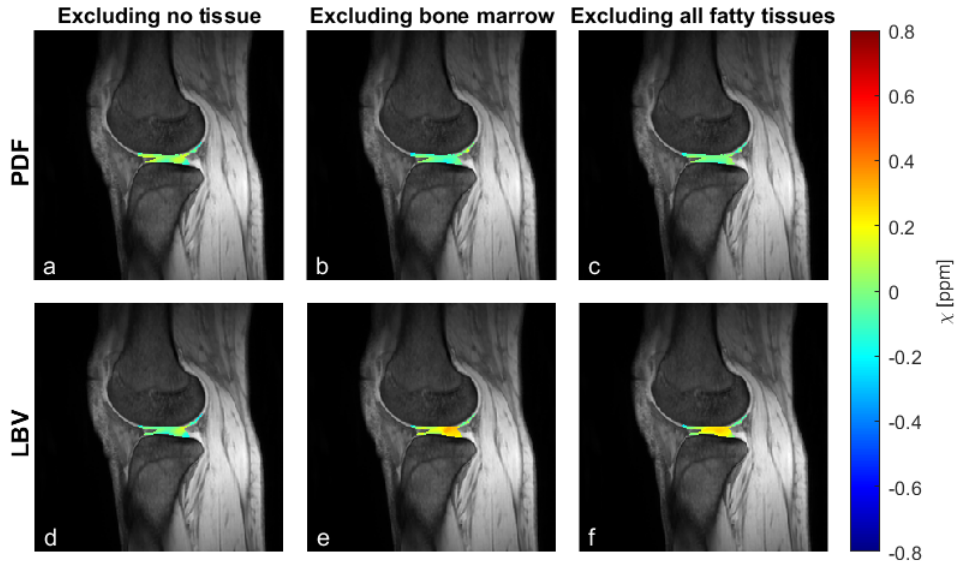

Figure 14: Susceptibility maps of the articular cartilage overlaid on magnitude images for context when (a, d) no tissue, (b, e) bone marrow and (c, f) all fatty tissue was excluded from the masks applied before the background field removal and dipole inversion step. The results obtained using PDF for background field removal are shown in (a-c) and those using LBV in (d-f).

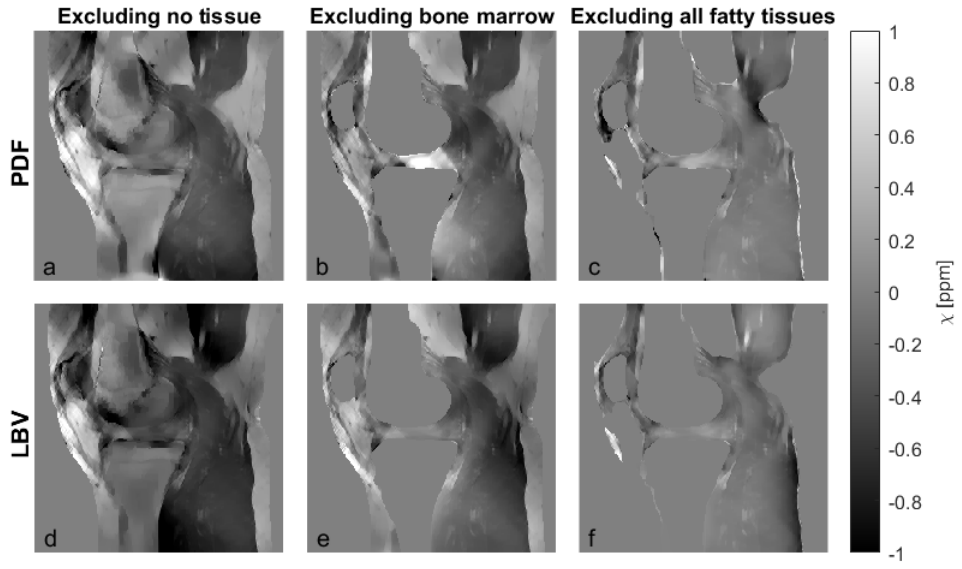

Figure 15: Susceptibility maps obtained from *in vivo* data of knee 2 with chemical shift removal when (a, d) no tissue, (b, e) bone marrow and (c, f) all fatty tissue was excluded from the masks applied before the background field removal and dipole inversion steps. The results obtained using PDF for background field removal are shown in (a-c) and those using LBV in (d-f). Streaking artefacts were seen when fatty tissue was not excluded from the reconstruction. These were reduced by exclusion of fatty tissue.

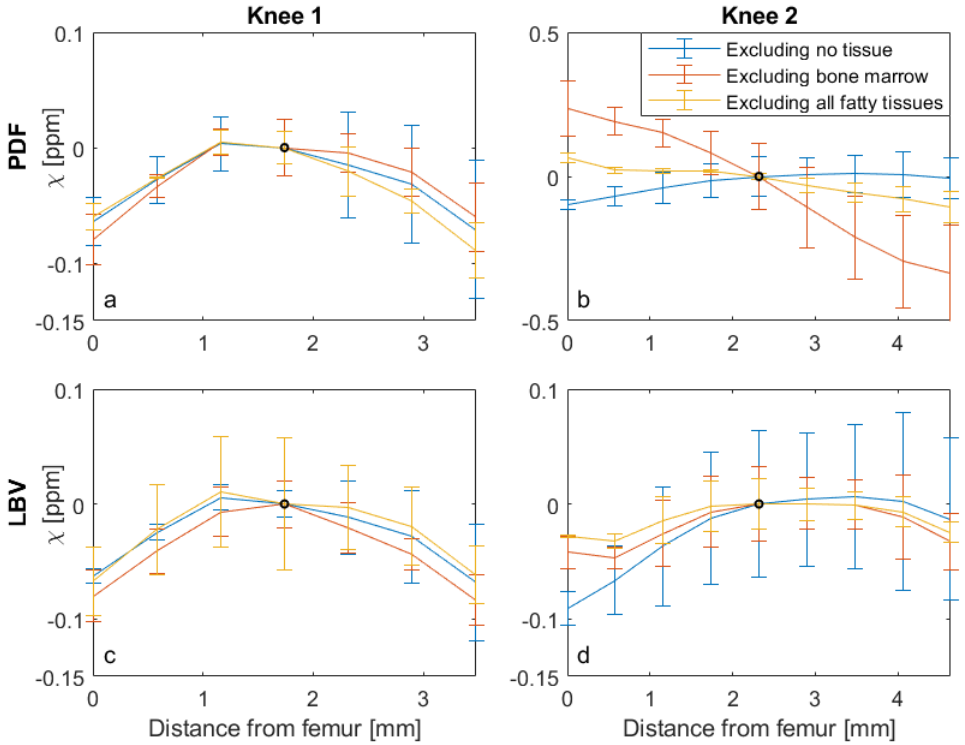

Figure 16: Profiles of the susceptibility values obtained over the area between the femur and tibia of knee 1 (a, c) and knee 2 (b, d) when the background field was removed using PDF (a, b) and LBV (c, d). The mid point between femur and tibia, which was assigned a zero susceptibility, is marked with a black circle. Bias was observed when fatty tissue was excluded from the reconstruction process in knee 2. Observe, that the results in (b) are presented using a larger y-scale than the others in order to show the whole profile for all masking alternatives.

5 Discussion

In this project, two approaches for handling the signal from fatty tissue in QSM, masking and CSEI, have been studied using both simulations and *in vivo* data. The effects of masking of fatty tissue has been evaluated with two potential sources of error in focus. First the possible information loss due to the exclusion of fatty tissue from the reconstruction process, and secondly, the effect of introducing edges close to the articular cartilage. Also, the effects of extreme values and residual chemical shifts in the total field map in case of CSEI, were visualized.

Further, simulations were compared to *in vivo* data. Here, reconstruction with and without CSEI was compared, as well as the effects of masking using two different background field removal techniques.

5.1 Simulations

The simulations indicate that the excluded tissue is at least partially accounted for in the background field removal step. This was seen particularly clearly in the area between the femur and tibia, where the local field was higher when bone marrow was included. A reason for this may be that fatty tissue is instead treated as a source of the background field when excluded. Likewise, this effect was illustrated when QSM was performed with matching and mismatching masks in the background field removal and dipole inversion steps. Here, a mismatch in the masks gave a less homogeneous susceptibility map. This indicates that the susceptibility of the fatty tissue cannot be considered as a source of the background field unless it is excluded from the reconstruction process in both of these steps.

However, bias was seen in the profiles extracted when masking of fatty tissue had been performed. This is thought to mainly stem from the introduction of edges close to the articular cartilage, but effects of incomplete removal of the magnetic field from the excluded tissue would also be included here. Generally, the most robust results were seen when no masking of fatty tissue was performed. In three previous *in vivo* studies, the range of susceptibility values over the articular cartilage was 0.2 - 0.3 ppm [6, 8, 10], while a fourth study presented a profile with larger differences, around 0.8 ppm [49]. Compared to these ranges, the bias seen in this work cannot be considered non-negligible.

The poorer performance of PDF compared to LBV when fatty tissue was excluded from the reconstruction process may be explained by the assumptions used in either method. Although PDF is widely used, especially in QSM of the brain, the technique includes a fundamental limitation, as the assumption of orthogonality is not true at the edges of the ROI, thus affecting accuracy of the technique in these regions. In contrast, LBV was shown to perform better in this aspect than PDF [30].

Interestingly, two cases showed smaller bias when all fatty tissue was excluded than when only bone marrow was excluded: PDF in knee 1 and LBV in knee 2. In the other cases, the results were comparable between these masking alternatives. This is somewhat surprising, as the bias would be expected to be at least the same between the two masking alternatives. One explanation may be that the fatty tissue in the first case is considered both a source of the background field and a source of the local field when only bone marrow is excluded. This might be challenging for the QSM reconstruction. Alternatively, the exclusion of all fatty tissues yields a susceptibility map which is easier to evaluate, as the ROI is completely homogeneous. This effect, however, was not studied, and a certain explanation can therefore not be given.

The simulations of error sources in the CSEI gave streaking artefacts in both cases, but with somewhat varying character. The results also gave an indication of what accuracy is needed in CSEI in order to avoid these streaking artefacts, as an offset of 0.01 ppm did not result in any visible streaking.

In the phantoms used for the simulations, four different materials were defined. These were chosen so that it would be possible to study the effects both of the exclusion of all fatty tissues and the exclusion of bone marrow only, as these are the strategies that have been employed in earlier studies in this area. Thus, the phantoms only included the most important parts for this project. Expanding the model used

for the simulations, by for example including a compartment for bone tissue, may be of interest for future works. With such a compartment, the effects of noise on the QSM reconstruction could be investigated in the relevant geometry. In this project, however, due to the low noise levels used, this was not relevant.

5.2 Analysis of in vivo images

The comparison of masking fatty tissue with and without first performing CSEI showed that masking of fatty tissue reduced the streaking artefacts in both cases. Without CSEI, however, the streaking artefacts were more severe. This suggests that chemical shift removal is advantageous, even if masking of fatty tissue is performed.

Although CSEI reduced streaking artefacts, residual artefacts were seen when fatty tissue was not removed. These streaking artefacts showed similarities to those seen when residual chemical shifts were simulated. This, in combination with the fact that masking of fatty tissue reduced or removed these artefacts suggest that they were caused by non-perfect CSEI.

The model describing the evolution of signal components of fat and water is relatively robust [27]. However, bias may occur in case of inaccuracies of the signal model. For example, bulk magnetic susceptibility effects, fast signal decay in bone tissue and temperature dependence of the chemical shift may result in incorrect reconstruction of ΔB. [46, 50] An approach for avoiding inaccuracies from such effects is to incorporate new information, e.g. about relaxation rate, in the signal model, or by iteratively updating the signal model [26, 50]. This was not done in the current project, but could be a way of improving the results of CSEI, and thus the estimation of susceptibility values.

The profiles extracted from the *in vivo* susceptibility maps, with two exceptions, had the expected shape with a maximum susceptibility in the superficial zones of the femoral and tibial cartilage. This agrees with theoretical predictions and results which have been obtained in earlier studies [6, 8, 10]. In the cases where the expected shape was not seen, artefacts were observed in the the reconstructed susceptibility maps, which might explaining the offset.

Similarities were seen when comparing the results obtained *in vivo* with those obtained through simulations. In knee 2, large biases were seen when PDF was used for background field removal in both masking cases. Furthermore, an offset between the results obtained with and without masking of fatty tissue was seen close to the femoral surface that corresponded well between simulations and in vivo data when LBV was used. Knee 2 was also seemingly more difficult to evaluate than knee 1 both *in vivo* and in the simulations. In knee 1, the results obtained using LBV agreed well between simulations and *in vivo* data, as the reconstruction yielded similar results using the different masking alternatives. Somewhat unexpected, on the other hand, was the results obtained when masking of fatty tissue was performed in combination with PDF in knee 1. From the simulations, a larger bias might be expected than what was seen in the *in vivo* case. Of course, the evaluation of bias is complicated in the *in vivo* case, as the ground truth is not known.

A difference between simulations and *in vivo* analysis is the ability to exclude fatty tissue completely. In the simulations, this could be done perfectly, as the compartments of each tissue was already defined, and could be used as a basis for the masks. In the *in vivo* images on the other hand, perfect correspondence between fatty tissue and areas excluded from the reconstruction process would be difficult to obtain. This has implications on the results obtained when comparing masking of fatty tissue with and without CSEI, as the artefacts seen when masking of fatty tissue was performed largely originated from areas where residual depots of fatty tissue might be present. Furthermore, the issue of imperfect masking of fatty tissue is of importance when discussing the application of QSM on the thin layer of articular cartilage. Here, masking of fatty tissue must be done with small margins as to not loose too much information about the tissue of interest. As such, QSM with fatty tissue excluded from the reconstruction process may be more difficult to perform with larger numbers of subjects, than QSM with fatty tissue included, as the personalized mask needed for each subject is more intricate. The risk of loosing cartilage volume due to imperfect masking is also larger when fatty tissue is excluded from the reconstruction process. Additionally, the masking of all

fatty tissues results in a mask with a larger number of edges, compared to the situations when only bone marrow is excluded or when fatty tissue is included. This, in turn, means that two different interests: 1) the exclusion of fatty tissue, and 2) the reduction of edges in the mask, may stand against each other using this technique. This complication may be avoided if a accurate enough correction of the chemical shift is developed, so that exclusion of fatty tissue may be avoided.

As was mentioned in the methods section, the values obtained from QSM are relative when not referenced to any tissue. In this projects, this circumstance did not pose a problem, as no inter-subject comparisons were performed. Currently, studies performing QSM of the articular cartilage have not referenced the obtained susceptibility values to any particular tissue, which, in practice, gives a result in reference to the mean susceptibility of the whole object. From these values, inter-subject comparisons have been made. Moving forward, it may be of interest to investigate alternative tissues or materials that may be used as a reference, similarly to how CSF is used as reference in brain imaging. This may, however, prove difficult, as no obvious such alternative exists in the knee.

A limitation of this project was that image data from only two individuals was used. Thus, the effect seen have not been possible to evaluate statistically. Moving forward, including a larger number of participants would be of interest. In this way, effects of the amount of subcutaneous fat could also be studied more extensively.

The evaluation of bias due to masking of fatty tissue rests mainly on the results obtained in the profiles over the cartilage area. The majority of the effects seen here are thought to originate from the introduction of edges close to the cartilage. However, as the effects of incomplete accounting for the susceptibility in the excluded areas were only evaluated qualitatively, the two effects cannot be completely separated from each other.

In this project, only one technique, MEDI, has been used for the dipole inversion step. This is an algorithm which is widely used in QSM, making it suitable to employ for the evaluations performed. However, other dipole inversion algorithms are available, which may be relevant to evaluate. For instance, it would be interesting to compare results using streaking artefact reduction for QSM (STAR-QSM) [51], as it has been used in several studies for the particular application of performing QSM in the knee.

Furthermore, some of the studies that excluded fatty tissue from the reconstruction process used fat saturation in the image collection [6,10]. Such data was not evaluated in the current study, meaning that no comparison between the collection techniques was made. The evaluated effects of excluding fatty tissue are not expected to differ between these image collection methods. However, a difference between these collection techniques is that fat saturation would not allow for CSEI to be performed. Considering the results obtained without CSEI and with exclusion of fatty tissue, QSM reconstruction based on data collected with fat saturation might be more susceptible to effects of imperfect exclusion of fatty tissue.

6 Conclusion

The simulations showed that the exclusion of fatty tissue from the reconstruction process introduces a bias in the resulting susceptibility maps. The size of this bias is dependent on both the choice of background field removal technique and the knee geometry.

In vivo, CSEI is required if fatty tissue is to be included in the reconstruction process. However, inaccuracies in this technique results in residual chemical shifts in the estimated total field perturbation map, which causes streaking artefacts. Exclusion of fatty tissue from the reconstruction process reduces these streaking artefacts, but introduces bias similar to that seen in the simulations.

Moving forward, further development of the model used in the CSEI is needed in order to avoid effects of residual chemical shifts in the estimated total field map.

References

[1] Hunter D, Bierma-Zeinstra S. Osteoarthritis. Lancet. 2019 Apr;393(10182):1745–59.

[2] Global, regional, and national incidence, prevalence, and years lived with disability for 310 diseases and injuries, 1990–2015: a systematic analysis for the Global Burden of Disease Study 2015. Lancet. 2016;388(10053):1545–602.

[3] Roemer FW, Demehri S, Omouni P, Link TM, Kijowski R, Saarakkala S. State of the Art: Imaging of Osteoarthritis. Radiology. 2020 Jan;296(1):5–21.

[4] Primorac D, Monar V, Rod E, Jeleč Ž, Čukelj F, Matišic´ V. Knee Osteoarthritis: A Review of Pathogenesis and State-Of-The-Art Non-Operative Therapeutic Considerations. Genes. 2020 Jul;11(8):854.

[5] Fox AJS, Bedi A, Rodeo SA. The Basic Science of Articular Cartilage: Structure, Composition, and Function. 2009 Nov;1(6):461–8.

[6] Wei H, Lin H, Qin L, Cao S, Zhang Y, He N, et al. Quantitative susceptibility mapping of articular cartilage in patients with osteoarthritis at 3T. J MagnReson Imaging. 2019 Jun;49(6):1665-1675.

[7] Dibb R, Xie L, Wei H, Liu C. Magnetic susceptibility anisotropy outside thecentral nervous system. NMR Biomed. 2017 Apr;30(4):10.

[8] Wei H, Dibb R, Decker K, Wang N, Zhang Y, Zong X, et al. Investigating Magnetic Susceptibility of Human Knee Joint at 7 Tesla. Magn Reson Mad. 2017 Jan;78(5):1933–43.

[9] Nykänen O, Sarin JK, Ketola JH, Leskinen H, te Moller NCR, Tiitu V, et al. T2* and quantitative susceptibility mapping in an equine model of post-traumatic osteoarthritis: assesment of machanical and structural properties of articular cartilage. Osteoarthr Cartil. 2019 Oct;27(10):1481–90.

[10] Zhang M, Yufei L, Feng R, Wang Z, Wang W, Zheng N. Change in Susceptibility Values in Knee Cartilage After Marathon Running Measured Using Quantitative Susceptibility Mapping. J MAGN RESON IMAGING. 2021 May;54(5):1585–93.

[11] Wang L, Nissi MJ, Toth F, Johnson CP. Quantitative Susceptibility Mapping Detects Abnormalities in Cartilage Canals in a Goat Model of Preclinical Osteochondritis Dissecans. Magn Reson Med. 2017 Mar;77(3):1276–83.

[12] Nykänen O, Rieppo L, Töjräs J, Kolehmainen V. Quantitative susceptibility mapping of articular cartilage: Ex vivo findings at multiple orientations and following different degradation treatments. Magn Reson Med. 2018 Dec;80(6):2702–16.

[13] Boehm C, Schlaeger S, Meineke J, Weiss K, Makowski MR, Karampinos DC. On the water–fat in-phase assumption for quantitative susceptibility mapping. Magn Reson Med. 2022 Nov;89(3):1068–82.

[14] Sharma SD, Hernando D, Horng DE, Reeder SB. Quantitative Susceptibility Mapping in the Abdomen as an Imaging Biomarker of Hepatic Iron Overload. Magn Reson Med. 2015 Sep;74(3):673–83.

[15] Blackburn TA, Craig E. Knee Anatomy - A Brief Review. Phys Ther. 1990 Dec;60(12):1556–60.

[16] Goldblatt JP, Richmond JC. Anatomy and biomechanics of the knee. Oper Tech Sports Med. 2003 Jul;11(3):172–86.

[17] Wei H, Gibbs E, Zhao P, Wang N, Cofer GP. Susceptibility Tensor Imaging and Tractography of Collagen Fibrils in the Articular Cartilage. Magn Reson Med. 2017 Aug;78(5):1683–90.

[18] Hunziker EB, Quinn TM, Häuselmann HJ. Quantitative structural organization of normal adult human articular cartilage. Osteoarthr Cartil. 2002 Apr;10(7):564–72.

[19] Schenk JF. Physical interactions of static magnetic fields with living tissues. Prog Biophys Mol Biol. 2005 Apr;87(2–3):185–204.

[20] Gaeta M, Cavallaro M, Vinci SL, Mormina E, Blandino A, Marino A. Magnetism of materials: theory and practice in magnetic resonance imaging. Insights Imaging. 2021 Dec;12(179).

[21] Brown RW, Cheng YCN, Haacke M, Thompson MR, Venkatesan R. Magnetic Properties of Tissues, Theory and Measurement. Second edition. Hoboken, New Jersey: John Wiley & Sons, Inc.; 2014.

[22] Schweser F, Deistung A, Reichenbach JR. Foundations of MRI phase imaging and processing for Quantitative Susceptibility Mapping (QSM). Z MedPhys. 2016 Mar;26(1):6–34.

[23] Liu C, Wei H, Gong NJ, Cronin M, Dibb R, Decker K. Quantitative Susceptibility Mapping: Contrast Mechanisms and Clinical Applications. Tomogr. 2015 Sep;1(1):3–17.

[24] Diestung A, Schweser F, Reichenbach JR. Overview of quantitative susceptibility mapping. NMR Biomed. 2017 Apr;30(4):e3569.

[25] Sharma SD, Artz NS, Hernando D, Horng DE, Reeder SB. Improving Chemical Shift Encoded Water-Fat Separation Using Object-Based Information of the Magnetic Field Inhomogeneity. Magn Reson Med. 2015 Feb;73(2):597–604.

[26] Dimov AV, Liu Z, Spincmaille P, Prince MR. Bone quantitative susceptibility mapping using a chemical species–specific signal model with ultrashort and conventional echo data. Magn Reson Med. 2018 Jan;79(1):121–8.

[27] Yu H, Shimakawa A, McKenzie CA, Brodsky E, Brittain JH, Reeder SB. Multiecho Water-Fat Separation and Simultaneous R2* Estimation With Multifrequency Fat Spectrum Modeling. Magn Reson Med. 2008 Nov;60(5):1122–34.

[28] Emini S, Oei EHG, Englund M, Peterson P. Imaging-based assessment of fatty acid composition in human bone marrow adipose tissue at 7 T: Method comparison and in vivo feasibility. Magn Reson Med. 2023 Feb;90(1):240–9.

[29] Liu T, Khalidov I, de Rochefort L, Spincemaille P, Liu J. A novel background field removal method for MRI using projection onto dipole fields (PDF). NMR Biomed. 2011 Mar;24(9):1129–36.

[30] Zouh D, Liu T, Spincemaille P, Wang Y. Background field removal by solving the Laplacian boundary value problem. NMR Biomed. 2014 Jan;27(3):312–9.

[31] Schmueli K, de Zwart JA, van Gelderen P, Li TQ, Dodd SJ, Duyn JH. Magnetic Susceptibility Mapping of Brain Tissue In Vivo Using MRI Phase Data. Magn Reson Med. 2009 Dec;62(6):1510–22.

[32] Liu T, Spincemaille P, de Rochfort L, Kressler B, Wang Y. Calculation of susceptibility through multiple orientation sampling (COSMOS): a method for conditioning the inverse problem from measured magnetic field map to susceptibility source image in MRI. Magn Reson Med. 2009 Jan;61(1):196–204.

[33] Wharton S, Schäfer A, Bowtell R. Susceptibility mapping in the human brain using threshold-based k-space division. Magn Reson Med. 2010 May;63(5):1292–304.

[34] Shmueli K, de Zwart JA, van Gelderen P, Li TQ, Dodd SJ, Duyn JH. Magnetic susceptibility mapping of brain tissue in vivo using MRI phase data. Magn Reson Med. 2009 Dec;62(6):1510–22.

[35] Liu J, Liu T, de Rochefort L, Ledoux J, Khalidov I, Chen W, et al. Morphology enabled dipole inversion for quantitative susceptibility mapping using structural consistency between the magnitude image and the susceptibility map. Neuroimage. 2012 Feb;59(3):2560–8.

[36] Kressler B, de Rochefort L, Liu T, Spincemaille P, Jiang Q, Wang Y. Nonlinear regularization for per voxel estimation of magnetic susceptibility distributions from MRI field maps. IEEE Trans Med Imaging. 2010 Feb;29(2):273–81.

[37] Liu T, Liu J, de Rochefort L, Spincemaille P, Khalidov I, Ledoux JR, et al. Morphology Enabled Dipole Inversion (MEDI) from a Single-Angle Acquisition: Comparison with COSMOS in Human Brain Imaging. Magn Reson Med. 2011 Sep;66(3):777–83.

[38] Worcester DL. Structural origins of diamagnetic anisotropy in proteins. Proc Nati Acad Sci. 1978 Nov;75(11):5475–7.

[39] Ruetten PPR, Gillard JH, Graves MJ. Introduction to Quantitative Susceptibility Mapping and Susceptibility Weighted Imaging. Br J Radiol. 2019 Mar;92(1101):20181016.

[40] Hopkins JA, Wehrli FW. Magnetic Susceptibility Measurement of Insoluble Solids by NMR: Magnetic Susceptibilitv of Bone. Magn Reson Med. 1997 Apr;37(4):494–500.

[41] Marques JP, Meineke J, Milovic C, Bilgic B, Chan KS, Hedouin R. QSM reconstruction challenge 2.0: A realistic in silico head phantom for MRI data simulation and evaluation of susceptibility mapping procedures. Magn Reson Med. 2021 Feb;86(1):526-542.

[42] Dong J, Liu T, Chen F, Zouh D, Dimov A, Raj A. Simultaneous Phase Unwrapping and Removal of Chemical Shift (SPURS) Using Graph Cuts: Application in Quantitative Susceptibility Mapping. IEEE Trans Med Imaging. 2015 Feb;34(2):531–40.

[43] de Rochefort L, Liu T, Kressler B, Liu J, Spincemaille P, Lebon V, et al. Quantitative susceptibility map reconstruction from MR phase data using bayesian regularization: validation and application to brain imaging. Magn Reson Med. 2010 Jan;63(1):194–206.

[44] Cornell MRI Research Group. MEDI toolbox, [computer program]; 2020, [cited date 25 april 2023]. Available from: http://pre.weill.cornell.edu/mri/pages/qsm.html

[45] de Rochefort L, Liu T, Kressler B, Liu jing, Spincemaille P, Lebon V, et al. Quantitative susceptibility map reconstruction from MR phase data using bayesian regularization: validation and application to brain imaging. Magn Reson Med. 2010 Jan;63(1):194–206.

[46] Szczepaniak LS, Dobbins RL, Stein DT, McGarry JD. Bulk Magnetic Susceptibility Effects on the Assessment of Intra- and Extramyocellular Lipids In Vivo. Magn Reson Med. 2002 Mar;47(3):607–10.

[47] de Rochefort L, Brown R, Prince MR, Wang Y. Quantitative MR susceptibility mapping using piece-wise constant regularized inversion of the magnetic field. Magn Reson Med. 2008 Oct;60(4):1003–9.

[48] Liu T, Wisnieff C, Lou M, Chen W, Spincemaille P, Wang Y. Nonlinear formulation of the magnetic field to source relationship for robust quantitative susceptibility mapping. Magn Reson Med. 2013 Feb;69(2):467–76.

[49] Zhang M, Li Z, Wang H, Chen T, Lu Y, Yan F, et al. Simultaneous Quantitative Susceptibility Mapping of Articular Cartilage and Cortical Bone of Human Knee Joint Using Ultrashort Echo Time Sequences. Front Endocrinol. 2022 Feb;13:844351.

[50] Dimov AV, Liu T, Spincemaille P, Ecanow JS, Tan H, Edelman RR, et al. Joint Estimation of Chemical Shift and Quantitative Susceptibility Mapping (Chemical QSM). Magn Reson Med. 2015 Jun;73(6):2100–10.

[51] Wei H, Dibb R, Zhou Y, Sun Y, Xu J, Wang N, et al. Streaking artifact reduction for quantitative susceptibility mapping of sources with large dynamic range. NMR Biomed. 2015 Oct;28(10):1284–303.